Journal of Industrial and Engineering Chemistry 133 (2024) 322–332

Contents lists available at ScienceDirect

Journal of Industrial and Engineering Chemistry

journal homepage: www.elsevier.com/locate/jiec

Ni supported on bioapatite for WGS: Improving catalyst stability and H_2 selectivity by Pt-doping and thermochemical activation of the support

U. Iriarte-Velasco [a], M.A. Gutiérrez-Ortiz [b], A.J. Reynoso [b,*], J.L. Ayastuy [b]

[a] Department of Chemical Engineering, Faculty of Pharmacy, University of the Basque Country UPV/EHU, Paseo de la Universidad, 7 01006, Vitoria, Spain
[b] Department of Chemical Engineering, Faculty of Science and Technology, University of the Basque Country UPV/EHU, Sarriena S/N 48940, Leioa, Spain

ARTICLE INFO

Keywords:
Bioapatite
Nickel
WGS
K_2CO_3
H_2SO_4

ABSTRACT

Catalytic properties of Ni and NiPt catalysts supported onto naturally derived hydroxyapatite (HAp) were investigated for the Water-Gas Shift (WGS) reaction in the 200–450 °C range. HAp was obtained by thermochemical conversion of waste animal bones which yield a porous solid mainly composed by apatite. A feed composition representative of real reformer outlet stream was used ($CO/H_2O/CO_2/H_2$ = 5/46/4/31 mol %) at a gas hourly space velocity of 120,000 h^{-1}. The catalysts were thoroughly characterised by N_2 physisorption, ICP-AES, H_2-chemisorption, XPS, FTIR, SEM-EDX, XRD, H_2-TPR, CO_2-TPD, and NH_3-TPD. From the light-off catalytic tests, it was found that all catalysts reached the equilibrium CO conversion in the 350–400 °C range. Pt doping into pristine Ni/HAp did not enhance neither catalytic activity nor selectivity to hydrogen. Interestingly, thermochemical activation (acid treatment) aimed to reduce the CH_4 formation (@ 350 °C) by around two-fold (25 % vs. 9–14 %) with a concomitant increase in the hydrogen yield. Moreover, catalytic stability was also improved. For instance, after 30 h TOS CO conversion dropped by 50 % for the pristine Ni/HAp and only 7 % for NiPt/SHAp catalyst. Similarly, the latter showed the highest and most stable hydrogen yield throughout all the long-term test.

Introduction

Waste-to-Energy has become a leading approach to solve waste disposal problems while harnessing the energy contained in its flue gases for electricity and heat production. The term "waste-to-energy" encompasses a large variety of biomass-based materials that can be processed by direct combustion, gasification, pyrolysis, or anaerobic digestion [1]. Both gasification and pyrolysis generate synthesis gas (syngas), a fuel consisting mainly of hydrogen, CO and CO_2, along with relatively small amounts of CH_4, N_2, and other impurities [2]. Water-Gas Shift (WGS) reaction is essential to upgrade conversion efficiency of this thermochemical processes, producing high-purity hydrogen from waste-derived syngas.

$$CO(g) + H2O(g) \leftrightarrow CO2\ (g) + H2\ (g) \quad (1)$$

$$CO(g) + 3H2\ (g) \rightarrow CH4\ (g) + H2O(g) \quad (2)$$

$$CO2\ (g) + 4H2\ (g) \rightarrow CH4\ (g) + 2H2O(g) \quad (3)$$

$$C(s) + 2H2\ (g) \leftrightarrow CH4\ (g) \quad (4)$$

$$2CO(g) \leftrightarrow C(s) + CO2\ (g) \quad (5)$$

WGS reaction (Equation (1) is an exothermic and reversible reaction, which is thermodynamically favoured at low temperature, and kinetically favoured at high temperature. Side reactions can also take place, leading to the formation of methane (Equation 2–4) and carbon via Boudouard reaction (Equation (5). Considering both thermodynamic and kinetic aspects, the industrial WGS reaction occurs in two stages, with different commercial catalysts in each one: high-temperature shift (HTS) at 350–550 °C using Fe-Cr oxide catalysts and low-temperature shift (LTS) at 190–250 °C with Cu-ZnO or precious metal-based catalysts [3]. Due to the high concentration of CO in waste-derived syngas, current catalysts for the HTS reaction are not suitable [4]. Furthermore, it is vital to find alternatives to replace chromium owing to its high human toxicity and negative environmental impact [5,6].

Nickel-based catalysts constitute an economically attractive alternative with almost comparable WGS activity with precious metal-based catalyst [7]. Nickel demonstrates unique performance in the WGS

* Corresponding author.
E-mail address: albertojose.reynoso@ehu.eus (A.J. Reynoso).

https://doi.org/10.1016/j.jiec.2023.12.003
Received 30 September 2023; Received in revised form 20 November 2023; Accepted 2 December 2023
Available online 10 December 2023

reaction, therefore is commonly utilized in processes like Steam Reforming, where WGS reaction plays a pivotal role [8–10]. The nickel catalysts exhibit excellent activity in the high-temperature WGS reaction and outperform other transition metal catalysts, including Co, Cu, and Fe, by achieving high CO conversion and hydrogen selectivity [11,12]. However, nickel-based catalysts usually have as major drawback for the WGS process the occurrence of methanation side reactions which reduce selectivity and yield to hydrogen [13]. Moreover, when the feed to the catalytic reactor contains hydrogen, as usually occurs in the reformer outlet stream, the production of the undesired methane is increased. At high temperature, catalyst deactivation by sintering is another limitation for nickel-based catalysts [14]. Several strategies such as, size control of the metal nanoparticles, control of the morphology and pore structure, creation of oxygen defects or tuning surface acidity/basicity have been used for the development of efficient, selective and stable catalysts in the WGS reaction [15]. Doping with small concentration of noble metals like to Pt for the formation of metal–metal interface active sites can improve the resistant to coking and sintering [16,17].

The characteristics of the catalyst support play an important role. Indeed, it is known that strong support-metal interaction can reduce sintering of the active sites during high temperature WGS reaction [18], whereas high basicity of support can favourably activate water molecule [19]. Moreover, the prevalence of weak acid and basic sites has been related to limited methanation [19–21]. Among the different strategies for surface acid-base tuning, a more facile and sustainable approach could be the use as support of bone char which contains heteroatoms (Cl, Mg, Na, etc.) [22]. Hydroxyapatite (HAp), readily and cheaply available from solid animal waste, has garnered attention as a catalyst support owing to its high thermal stability, abundant oxygen vacancies, and adjustable acid and basic sites [23]. It is a compact assemblage where Ca^{2+} ions and tetrahedral $[PO_4]^{3-}$ groups delimit two unconnected channels. The first one (2.5 Å in diameter) contains Ca^{2+} (I) ions surrounded by oxygen atoms. The second type has a diameter of 3.5 Å and hosts the hydroxyl groups and Ca^{2+} (II) cations. The structure of apatite is very flexible and can be replaced by a large number of other metal ions through ion exchange, without affecting the crystalline structure [24]. Several studies have reported on the outstanding performance of WGS on HAp-supported catalysts [25,26]. The suitability of HAp for WGS reactions may be credited to the superior activation of water molecules on Lewis acidic calcium cation and H-bonding to basic oxygen atoms from phosphate ion. In addition, HAp support ensures that active sites remain highly resistant to sintering [27].

In this work, a catalyst with Ni supported onto hydroxyapatite of natural origin thermochemically activated was employed. The ion exchange ability of the HAp was employed to alleviate the stability issue. As a result, development of an environmentally sustainable strategy to promote WGS activity and selectivity to hydrogen is the main challenge of this work.

The natural apatite was synthesized by a one-step thermochemical activation of waste animal bone, using either H_2SO_4 or K_2CO_3, and then Ni was loaded by wet impregnation. Pt was added as a second active metal to promote the WGS performance. The promotion effect of Pt doping on the chemically activated and non-activated bone char was studied in depth. Thus, this study explored for the first time the potential of the combination of Ni-Pt synergy over thermochemically activated hydroxyapatite support for the efficient and clean production of hydrogen.

Experimental

Catalyst synthesis

The support was prepared from pork chop bones collected from a local butcher shop. First, bones were cleaned from meat, cut into pieces of 2–5 cm and precalcined in air flow (120 NmL/min), heating at 5 °C/min to 500 °C and hold for 2 h. The obtained biochar was sieved and particles in the 0.09–0.25 mm size range were selected. This material will be referred as precursor (HAp). The precursor was modified by chemical treatment by either H_2SO_4 (S) (at 0.2 $mmol_{H2SO4}/g$) or K_2CO_3 (K) (at 5 $mmol_{K2CO3}/g$). Supports were treated overnight, filtered and then heated in air flow at 550 °C for 2 h. These activation conditions were set based on previous experience [28].

Activated supports were loaded with Ni and Pt (10 wt% Ni; 1 wt% Pt loadings) by successive impregnation method, using aqueous solutions of $Ni(NO_3)_2{\cdot}6H_2O$ and $Pt(NH_3)_4(NO_3)_2$. The precursor was firstly impregnated with the solution of Ni, dried overnight at 110 °C. For the bimetallic catalysts, this procedure was repeated for the deposition of the Pt. Finally, the solids were calcined in air flow at 450 °C for 2 h. As a reference, monometallic (Ni/HAp) and bimetallic (NiPt/HAp) was prepared using pristine HAp support. Overall four catalysts formulations were prepared (Ni/HAp, NiPt/HAp, NiPt/KHAp, NiPt/SHAp). Further information on reagent chemicals and catalyst preparation (Scheme S1) is provided in the ESI.

Catalyst characterisation

The bulk chemical composition of the solids was evaluated by ICP-AES (Horiba Yobin Yvon Activa). BET method was used to determine the specific surface area, while the average pore size, total pore volume and pore size distribution (PSD) were estimated based on the BJH method from the N_2 desorption branch (analysis carried out in a Tristar II 3020 equipment).

The crystalline structures and the variation in the unit cell dimensions of the catalysts was analysed by XRD (Philips PW1710 diffractometer) using the ICDD database to the identification of the phases. The Rietveld method was used for microstructure analysis (profile refinement) and for the estimation of the unit cell parameters. The crystallinity of the solids was calculated from the full width at half maximum of (0 0 2) reflection of hydroxyapatite [29].

The identification of the reducible species and their interaction with support were examined by temperature-programmed reduction (H_2-TPR) (Micromeritics Autochem 2920 apparatus). The exposed metal surface area was determined by H_2 chemisorption in a Micromeritics ASAP 2020. Surface functionalities were analysed by Fourier transform infrared spectroscopy (FTIR) transmission spectra using disks of samples diluted in KBr (Nicolet Protege 460). The oxidation state of surface metal active sites was studied by X-ray photoelectron spectroscopy (XPS) (Phoibos 150 1D-DLD, monochromatized Al Ka, 1486.7 eV, X-ray radiation) in both calcined and reduced form of catalysts. The surface acid and basic site density was measured by ammonia/carbon dioxide pulse chemisorption and subsequent NH_3-TPD and CO_2-TPD (Micromeritics Autochem 2920). The catalyst surface morphology and metal dispersion was analysed by Scanning electron microscopy coupled with energy dispersive spectroscopy (FEG-SEM-EDX) on a JEOL JSM-7000F apparatus. More details on analytical methods are given in ESI.

Catalytic performance

The WGS performance of the catalyst was studied in a downflow fixed bed stainless steel reactor (D_i = 13.3 mm; length = 305 mm) (Scheme S2, ESI). Prior to reaction, the catalyst (0.1 g diluted in silicon carbide particles of the same size, to achieve 1 mL volume) was in-situ reduced under 15 % H_2/He flow at 400 °C for 1 h. Then, the reactor was cooled down to 200 °C under He flow and the feed stream was introduced. Deionized water was supplied by HPLC pump (Gilson 307), and vaporized at 150 °C before mixing with reactant gases. Catalyst activity tests were carried out at atmospheric pressure in the 200–450 °C range, with a total flow rate of 200 mL/min STP (GHSV = 120,000 h^{-1}). The feed composition was $CO/H_2O/CO_2/H_2/He$ = 5/46/4/31/14, representative of a realistic reformer outlet stream. A Peltier device was used to condense the unreacted water from the reactor outlet stream before routing the non-condensable products to an μGC (Agilent 490,

with two molecular sieves with He and Ar carriers, respectively, and one PPQ column with He carrier) equipped with a TCD detector. Samples were collected once steady state at each temperature was attained. Stability tests (duration 24 h) were carried out at isoconversional conditions (X_{CO} = 70–80 %, T = 325 °C for pristine catalysts; 350 °C for the chemically treated samples).

The CO conversion and yields (Y_i) to H_2 and CH_4 were calculated according to equations (1)-(3):

$$X_{CO}(\%) = 100 \times \frac{F_{CO,in} - F_{CO,out}}{F_{CO,out}} \quad (6)$$

$$Y_{H2}(\%) = 100 \times \frac{F_{H2,out}}{F_{CO,in}} \quad (7)$$

$$Y_{CH4}(\%) = 100 \times \frac{F_{CH4,out}}{F_{CO,in} + F_{CO2,in}} \quad (8)$$

C selectivity was defined as:

$$C_{selectivity}(\%) = 100 \times \frac{F_{C,in} - F_{C,out}}{F_{C,in}} \quad (9)$$

Results and discussion

Chemical composition and textural properties

Table 1 shows ICP data and textural and morphological results. The Ni and Pt content was close to theoretical value in the bare support whereas it was slightly lower in the chemically treated assays. The bare support (HAp) had a molar Ca/P ratio of 1.64, slightly lower than the stoichiometric value for pure hydroxyapatite (Ca/P = 1.67) because of the natural appearance of Ca-deficient phases such as β-tricalcium phosphate [30]. Acid-treated sample showed the highest deviation and the lowest Ca/P ratio of 1.61. It is well known the capacity of apatites to replace Ca^{2+} by other cations [31]. This result suggested that Ca ions in the apatite were more readily substituted by other cations and/or leached out after acid treatment of bone char. High acidity could favour local surface dissolution of the natural apatite, and thus enhance the cationic exchange between Ca^{2+} and Ni^{2+}/$Pt\delta^{+}$.

The N_2 adsorption–desorption isotherms of all catalysts (Figure S1, ESI) showed a similar typology of isotherm and hysteresis loop (Type II, H3) which suggested a plate-like layered structure with open pores on the mesopore and macropore scale. The distribution of pores obtained from the analysis of these isotherms are reported in Table 1 and Figure S1b (ESI). Pt-doping in the reference catalyst (Ni/HAp) hardly modified the PSD with a resultant S_{BET} of around 62 m^2/g, a pore volume of 0.28 cm^3/g, and average pore size of 15.4 nm. The chemical treatment of the support can significantly affect its textural properties [32]. As observed, the S_{BET} of the developed catalysts decreased (by 26–39 %), and the main peak of pore size distributions significantly upshifted (from c.a. 15 nm to c.a. 26–29 nm), indicating a pore widening in the mesoporous range. Interestingly, after catalyst reduction in hydrogen flow, the S_{BET} and pore volume (Table 1) increased by around 12–20 % for the non-chemically activated catalysts (Ni/HAp, NiPt/HAp), however, it increased by roughly 5 % for the chemically activated catalysts (NiPt/KHAp and NiPt/KSAp). These results showed that the applied chemical treatment conferred morphological stability to the developed catalysts, since textural properties hardly varied upon reduction in hydrogen flow.

Study of the surface morphological characteristics

The crystalline structure of the support and Ni particles was investigated using XRD. The diffractograms of the freshly calcined, reduced and exhausted samples are reported in Fig. 1. It can be observed that characteristic peaks of apatite phase were prominent in the bare support (precursor) and in all the prepared catalysts at around 2θ of 26.0, 32.0, and 33.0°. Characteristic peaks of NiO at 37.2° and 43.3° were observed in the calcined form of catalysts. No peaks due to Pt or PtOx phases were detected, likely due to low amounts of Pt (0.4–0.8 wt%) and below detection limit size of nanoparticles. Pt-doping into the reference catalyst did not affect the position of the HAp diffraction peaks (Fig. 1a). For

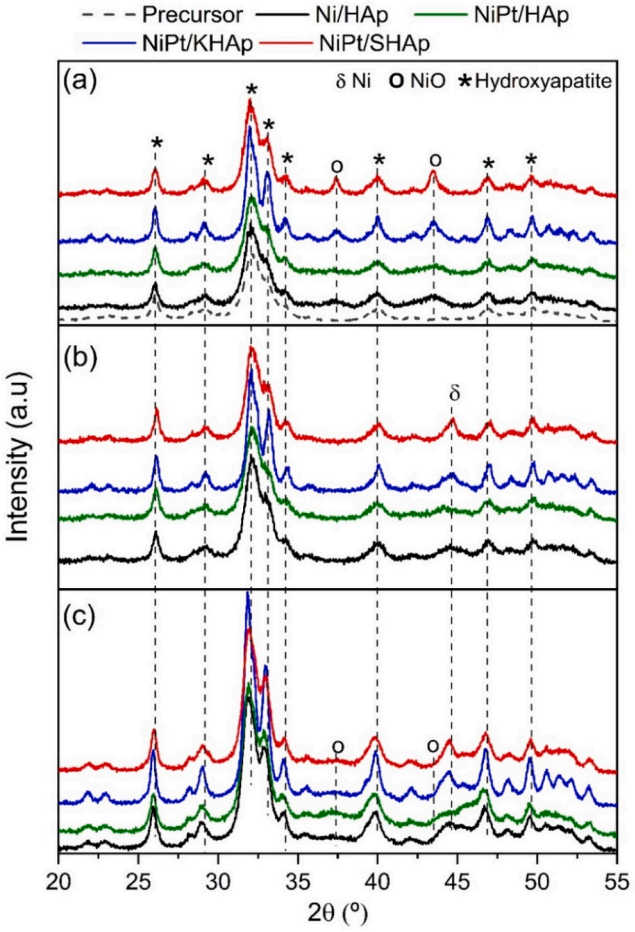

Fig. 1. XRD patterns for bone char supported catalysts (a) Calcined, (b) Reduced, and (c) Spent catalyst.

Table 1
Chemical, textural and structural properties of the catalysts.

Catalyst	Metal loading [a] (wt.%)		Ca/P [b]	S_{BET} [c] (m^2/g)	V_P (cm^3/g)	d_P (nm)	d^d_{HAp} (nm)	d^e_{NiO} (nm)		d^f_{Ni} (nm)	Spent catalysts	
	Pt	Ni						(111)	(200)		$d_{NiO(111)}$ [g] (nm)	$d^{o,g}_{Ni}$ (nm)
Ni/HAp	n.a.	9.6	1.64	61.8 (69.0)	0.289 (0.323)	16.1 (17.1)	9.2 (10.1)	7	4	5	13	5
NiPt/HAp	0.8	9.1	1.64	62.1 (75.8)	0.275 (0.329)	15.4 (15.3)	10.3 (9.8)	8	3	7	6	9
NiPt/KHAp	0.5	7.7	1.65	37.8 (39.2)	0.288 (0.302)	28.6 (31.1)	16.5 (20.7)	12	7	6	4	10
NiPt/SHAp	0.8	7.9	1.61	45.5 (48.3)	0.321 (0.343)	26.1 (26.9)	14.3 (9.7)	46	10	12	5	13

In parenthesis values measured after reduction at 400 °C; n.a.: not analysed; [a] from ICP-AES; [b] mol/mol; [c] from nitrogen isotherms; [d,e] from XRD (*hkl*); [f] from XRD, plane (1 1 1) of the reduced samples; [g] from XRD of used catalysts in long term WGS reaction

instance, the peaks corresponding to the (1 1 2) and (3 0 0) reticular planes, at 32.07° and 33.00° for the precursor and catalysts Ni/HAp and NiPt/HAp hardly varied.

The 2θ values obtained by the Rietveld refinement (Table S1, ESI) were slightly higher than those of stoichiometric hydroxyapatite (ICDD 01–84-1997, Ca/P = 1.67, a = b = 9.4180, c = 6.8840). Because of the natural origin and the coexistence of other heteroatoms (Table S2, ESI) in our samples, which produced a calcium-deficient hydroxyapatite (Ca/P = 1.61–1.64), the lattice parameters measured for our naturally derived HAp (a = b = 9.40809, c = 6.8783) were smaller than pure hydroxyapatite. This suggested that smaller atoms (i.e. Na, Mg) were more readily exchanged with Ca^{2+}.

The lattice parameters and cell volume remained similar after loading of Pt (Table S1, ESI). Therefore, it seems that the Pt species mainly spread on the HAp surface with very little incorporation into the HAp structure. After reduction at 400 °C, a slight decrease in the HAp cell parameters of Ni/HAp and NiPt/HAp was observed which caused a decrease in the apatite lattice volume of around 0.25 % (from 528.7 to 527.5 $Å^3$).

Regarding the catalysts supported on the chemically treated apatite, their XRD diffractograms showed a clear displacement in the position of 2θ corresponding to (1 1 2) and (3 0 0) planes of HAp. Similarly, the characteristic diffraction peaks of the NiO phase were also affected. Moreover, lattice expansion was higher than that observed for the reference catalyst (Table S1, ESI), supporting the partial incorporation of these cations into the apatite framework [27,33]. This observations point out that the chemical treatment modified the cell parameters of the naturally obtained apatite, and also the interaction between the incorporated Ni, and likely Pt, species with the support. Interestingly, after reduction the cell parameter of the chemically treated supports varied to a lesser extent as compared to the non-treated assays. Therefore, in line with observation of the textural data, it seemed that chemical activation enhanced the chemical stability of the natural apatite supported catalysts.

The Scherrer's equation was applied to XRD diagrams to estimate crystal sizes of the supported species. As can be deduced from data in Table 1, NiO crystallites were detected on the surface of the reference catalyst. Note that these crystallites were longer in horizontal growth direction than vertical (i.e. 7 nm vs. 4 nm). Also, values of catalyst NiPt/HAp reflected that Pt doping did not affect growing of NiO crystallites. Regarding the chemically treated samples, for instance, catalyst NiPt/KHAp contained NiO crystallites of larger size (12 nm x 7 nm) as compared to the reference catalyst Ni/HAp. Interestingly, the largest NiO particles were formed on the surface of the acid treated sample (NiPt/SHAp), with a particularly enhanced growing in the horizontal plane (46 nm x 10 nm). After reduction in hydrogen flow, no characteristic XRD peaks of NiO were observed and a new peak, characteristic of metallic Ni, appeared at around 2θ = 43.5 °. The average crystal size of metallic nickel was of around 5–7 nm in catalysts Ni/HAp, NiPt/HAp and NiPt/KHAp. However, catalyst NiPt/SHAp contained Ni^0 crystallites of around 12 nm. Thus, it seemed that the treatment of the natural HAp with acid affected growing geometry of deposited NiO particles, with preferential horizontal growing, which produced the largest Ni^0 particles upon reduction (i.e. two-fold increase in size). This trend suggests that the larger size of metallic Ni particles is most probably due to differences in the type of interaction Ni-Pt-HAp compared with that in the non-treated support. As will be discussed in the reducibility section, catalyst NiPt/SHAp contained a broad peak at the highest temperature due to deposition of reducible Ni-Pt species with a relatively strong interaction with support.

SEM images of the fresh catalysts (Figure S2, ESI) showed that the morphology at micrometre scale consists of a combination of smooth and rough surfaces and folds appear on the surface together with granular material. The distribution of the different elements on the surface of fresh catalysts was performed by EDX dot mapping images (Figure S3, ESI), in which a higher concentration of species appears brighter. This revealed that the metallic species were well distributed on the surface of the bone char support. Moreover, particles detected by EDX analysis of the bimetallic catalyst demonstrated the presence of Ni, O and Pt enriched regions. Interestingly, the coexistence of Mg can be also observed. The deposition of nickel particles could promote the formation of particles of the second active metal. The superimposition of loaded metals onto hydroxyapatite was also observed by others [34]. Contrarily, as can be observed, the active metals are located in Ca, P and C lean areas.

Reducibility and metallic function

The reference catalyst showed the highest amount of exposed Ni atoms on the surface (Table 2). The metallic sites density decreased by around 25 % after Pt doping, from 1.12 to 0.79 sites per nm^2. The sample activated with the alkali showed a similar metallic sites density. However, a significant decrease was observed in the acid treated catalyst (i.e. 0.41 metal sites per nm^2). This result is fully consistent with the favoured growth of the metallic Ni nanoparticles measured by XRD for catalyst NiPt/SHAp.

Fig. 2 shows the H_2-TPR profiles of the calcined catalysts. The reduction profile of the support showed no reduction peak at below 500 °C, which was the maximum heating temperature used to obtain the natural apatite used as support. Hydrogen consumption at above 500 °C could be ascribed to apatite dehydroxylation reactions [35]. The H_2-TPR profile of the reference catalyst Ni/HAP could be differentiated into six hydrogen consumption peaks. The low temperature peaks centred at 185 °C and 285 °C can be assigned to reduction of NiO particles with weak interaction with the support [36]. The prominent peak centred at 360 °C was assigned to the reduction of nickel species having mild interaction with the support (i.e. NiO particles identified by XRD). Upon integration of these three peaks a H_2/Me molar ratio of 0.57 was measured (Table 3). Thus, in line with XRD and XPS data, the partial reduction of the NiO species was evidenced after reduction in hydrogen flow at 400 °C. Note that the overall hydrogen consumption up to 500 °C (the support stabilization temperature) was very close to the stoichiometric value (H_2/Me = 0.997). The hydrogen consumption peaks at higher temperatures could not be unambiguously assigned. Previous reports on nickel supported onto hydroxyapatite suggested the reduction of: (i) NiOx species with strong interaction with the support; (ii) ion exchanged Ni^{2+} in the Ca^{2+} sites of the apatite; and (iii) the dehydroxylation of the apatitic support [37,38]. The above mentioned stoichiometric consumption, suggested that the latter process was the most probable.

The profile of the Pt-doped catalyst (NiPt/HAp) was comparable with that of the reference catalyst with two main reduction events, being the most prominent that at the higher temperature (320 °C). However, the peaks appeared shifted to lower temperatures (i.e. 230/320 vs. 285/360 °C). The integration values summarised in Table 3, revealed a H_2/Pt value of 11, what indicates the reduction of all surface PtOx species with weak interaction with the support. Boukha et al. [27] reported that Pt could be incorporated into the HAp structure, however, in our naturally derived apatite, this behaviour seemed unlikely. XRD data showed no modification of cell parameters upon Pt loading. Moreover, the above mentioned H_2/Pt mole ratio suggested that reduction of additional species took place. Several authors have reported that the reduction of bulk nickel oxide can occur at lower temperatures in the presence of Pt, as due to the spillover on metallic Pt [39–41]. As observed from SEM images, Pt and Ni were deposited on catalyst surface in close interaction. Thus, it seemed likely the occurrence of hydrogen spillover from Pt to the adjacent Ni particles what would facilitate its reduction. Furthermore, the reduction of oxygen functionalities on the support itself could not be discarded based on the larger than stoichiometric hydrogen consumption of these catalysts (H_2/Me = 1.12–1.52) [42].

The activation of the apatitic support with acid did not significantly affect the position of the low temperature peak (c.a. 230 °C) as

Table 2
Surface chemical properties and kinetic parameters of the catalysts.

Catalyst	Accesible metallic sites [a] ($at_{Me}./g$)($\times 10^{-18}$)	Acid sites density [b] (sites/nm^2)	Basic sites density [b] (sites/nm^2)	Basic/acid site ratio	Surface unidentate carbonate to CO_3^{2-} [c]	T_{50} [d] (°C)	r_{CO} [e] ($\mu mol_{CO}/g/s$) @275 °C	TOF (s^{-1}) @275 °C
Ni/HAp	77.1	0.93	0.57	0.61	0.12	316	4.0	0.03
NiPt/HAp	59.8	1.17	0.51	0.43	0.11	300	6.7	0.07
NiPt/KHAp	54.2	0.37	0.82	2.19	0.27	325	4.0	0.04
NiPt/SHAp	19.7	0.90	0.48	0.53	0.08	335	3.2	0.10

[a] H_2 pulse chemisorption; [b] Temperature-programmed desorption (NH_3-TPD; CO_2-TPD).[c] from FTIR spectra peak integration at 1385 cm^{-1} vs 1415–1461 cm^{-1}; [d] Temperature to reach 50 % conversion of CO; [e] WGS reaction at isoconversion conditions (75 % CO conversion @325–350 °C).

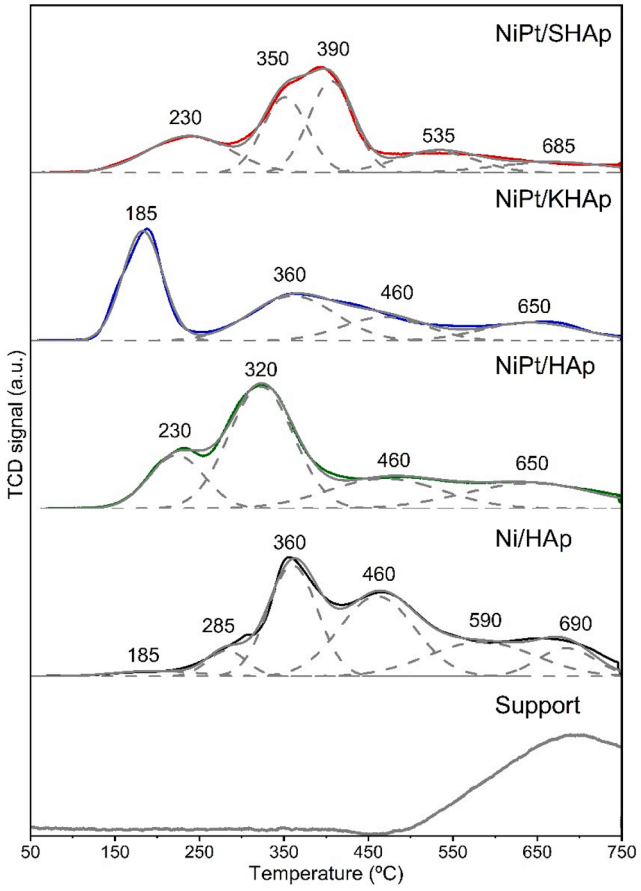

Fig. 2. H_2-TPR profiles of fresh calcined catalysts.

compared to the non-chemically treated bimetallic catalyst. Moreover, the amount of species reducible at T < 300 °C remained similar (uptake 0.42 vs. 0.50 $mmol_{H2}/g$). The resulting H_2/Pt mole ratio for the latter samples was 7 and 11, respectively. Thus, the concomitant reduction of Pt and Ni species was likely to occur. Indeed, the decrease in the reduction temperature of the nickel species could be ascribed to PtOx-NiO interactions.

The reduction profile of the sample activated with alkali (NiPt/KHAp) was the most dissimilar among the prepared catalysts. It showed an intense peak at 185 °C, which reflected the existence of an increased amount of easily reducible species on the catalyst surface. As for the previous catalysts, the concomitant reduction of Pt-Ni species is likely to occur. However, the H_2/Pt mole ratio (H_2/Pt = 24) was notably increased. This suggested an abundance of other species, apart from the loaded metals, existing on the catalyst surface as a consequence of the alkali treatment, that were also reduced. Indeed, additional hydrogen spillover from Pt to the support surface could take place. The total H_2/

Table 3
H_2-TPR data for the catalysts.

Catalyst	H_2 uptake ($mmol_{H2}/g$)			T (°C)
	T < 500 [a] (H_2/Me)	T < 300[b] (H_2/Pt)	(H_2/Me)	
Ni/HAp	1.63 (0.997)	0.20 (n.a.)	0.07 (0.04) 0.13 (0.08)0.73 (0.45)	185 285 360
NiPt/HAp	2.18 (1.41)	0.50 (11)	0.50 (0.31) 1.28 (0.81)	230 320
NiPt/KHAp	2.00 (1.52)	0.93 (24)	0.93 (0.69) 0.77 (0.57)	185 360
NiPt/SHAp	1.50 (1.12)	0.42 (7)	0.42 (0.30) 0.45 (0.33)0.56 (0.40)	230 350 390

[c] Likely, includes intense dehydroxylation.
[a] In brackets, H_2/Me ratio. Calculated using T = 500 °C integration cut-off method by finite increments.
[b] Caculated by integration of deconvolution peaks up to T °C.

Me mole ratio was highest for this catalyst (1.52), what supports this scenario.

In summary, from H_2-TPR data it can be concluded that Pt promotion significantly increased the reducibility of $Ni^{\delta+}$ species (low temperature H_2 consumption increased two-fold from 0.2 $mmol_{H2}/g$ in the reference catalyst to 0.42–0.49 in NiPt/HAP and NiPt/SHAp, respectively). H_2 consumption in catalyst NiPt/KHAp occurred at the lowest temperature (185 °C), likely due to carbonates deposition on catalyst surface after the alkali activation. Interestingly, the acid treated sample, NiPt/SHAp, showed a broad multipeak feature in the 350–390 °C range what would imply that the NiO species in close interaction with the support exhibited a wider size distribution with a larger average size, in accordance with XRD data.

Structure and coordination state

The analysis by FTIR (Figure S4, ESI) showed the characteristic bands for phosphate ion at 1093, 1035, 961, 603, 563, and 473 cm^{-1}. Table S3 (ESI) lists the wave numbers and their corresponding vibration modes for the different species found in the samples. The bands at around 3440 and 1637 cm^{-1} were assigned to the bending mode of the adsorbed water, whereas the peaks at 3570 cm^{-1} and 633 cm^{-1}, corresponding to OH bands of HAp, were clearly visible for the treated samples. The existence of carbonates (1461, 1415, 1385, and 870 cm^{-1}) was confirmed in all samples. An unresolved weak doublet representative of A-type (hydroxyl substituted carbonate ions) at 880 cm^{-1} [43] and B-type (phosphate substituted carbonate ions) at 870 cm^{-1} [44] in the HAp structure was observed in our samples. Moreover, the alkali treated sample showed the most intense signal at around 1385 cm^{-1} which has been associated to the transformation of free carbonates into

surface unidentate carbonates [45]. From the FTIR spectra, the amount of unidentate surface carbonates was 2.3 times higher for NiPt/KHAp as compared to the reference catalyst. It is likely that the reduction of such species would contribute to the observed prominent reduction peak at around 185 °C, discussed in H_2-TPR.

XPS was used to study the chemical composition and the oxidation state of elements on the catalysts surface. The survey spectrum of the calcined catalyst showed that O, Ca, P and Ni were the main elements. The presence of C was evidenced by peaks at BE values characteristic of aliphatic 284.6 eV (C–H, C–C) and aromatic 289.1 eV (O-C = O) carbonaceous material (Table S4, ESI). It accounted for around 4 at.%, except for the alkali treated sample, which contained a significantly larger amount of C (i.e. 8 at.%), mainly due to aliphatic carbon. Content of K and Na was below 2 at.%. Some Mg 2 s could be identified, though close to method detection limit. Pt was identified in the surface of doped samples at concentrations of around 0.05 at.%. In the reduced samples, all same elements could be identified on catalyst surface, with the exception of C, which was removed upon reduction. The surface Ca/P

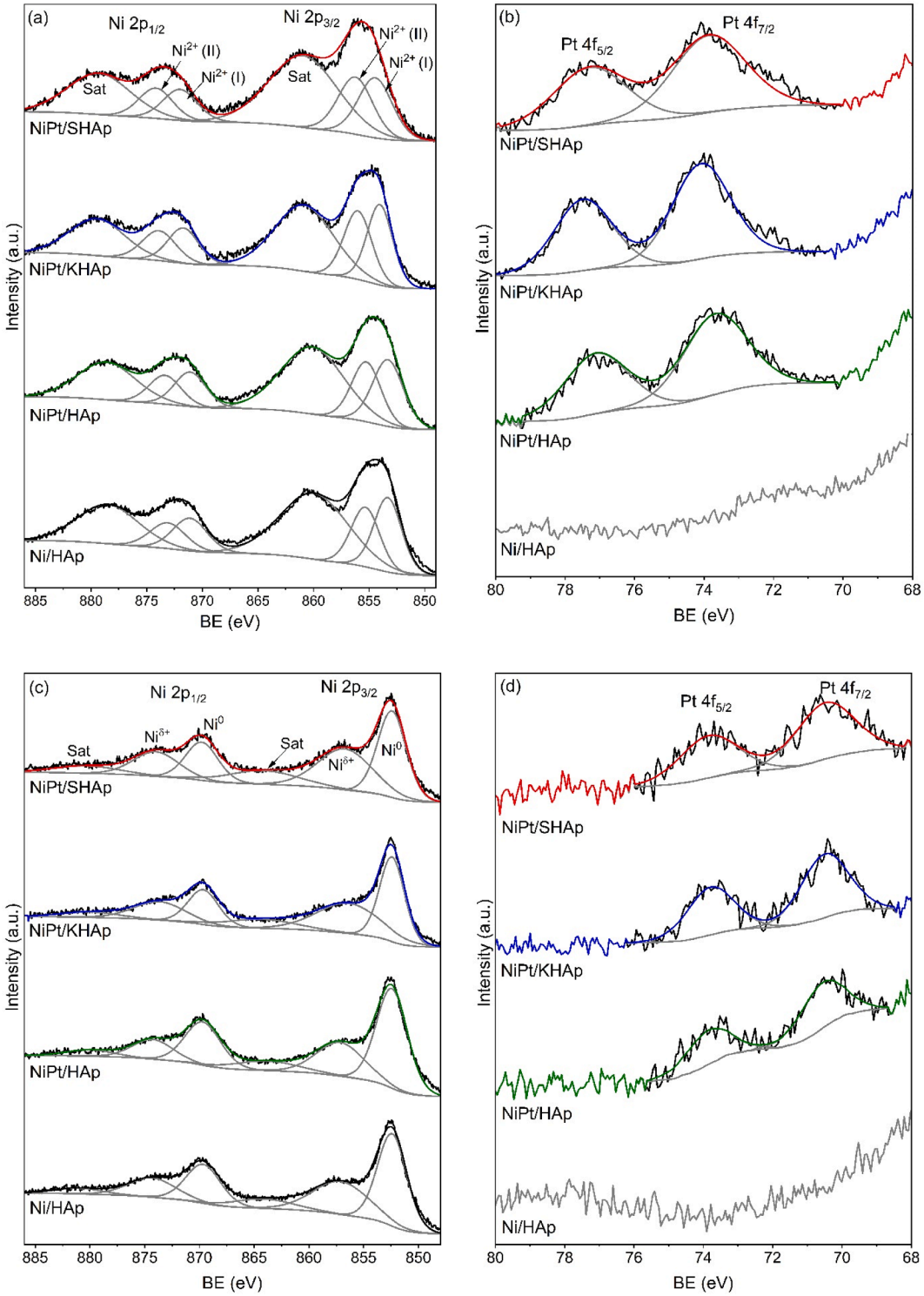

Fig. 3. XPS spectra of Ni 2p and Pt 4f of (a,b) calcined and (c,d) reduced catalysts.

atomic ratio (1.3–1.4, Table S4, ESI) was notably lower than the bulk value (1.6) what suggested a lower amount of exposed Ca atoms in surface. These results suggested that the loaded Ni and Pt could be deposited preferably over the surface Ca sites.

The high-resolution XPS spectra were used to analyse nickel and platinum speciation. Fig. 3a shows the Ni $2p_{3/2}$ spectra for the calcined catalysts. For the reference catalyst, the main photoemission peak can be deconvoluted into two peak at 853.3 and 855.3–856.2 eV and a broad satellite structure appearing at around 860 eV. In agreement with previous studies these are consistent with the presence of NiO particles with weak and strong interaction with the support, respectively. The low BE peak can be attributed to the binding energy of Ni $2p_{3/2}$ in NiO dispersed on the phosphate [46]. The second peak at around 855.7 eV was ascribed to NiO particles with a stronger interaction with the support [47]. On the other hand, Boukha et al. [38] observed an analogous peak at higher binding energies (856.9 ± 0.3 eV) which was ascribed to ion exchanged Ni^{2+} in the Ca^{2+}(I) and Ca^{2+}(II) sites of the apatite. In the spectra of the NiPt/KHAp and NiPt/SHAp catalysts the higher BE peak appears at 856.0–856.2 which might be associated to the partial exchange of the Ni^{2+} atoms in the apatite structure.

Fig. 3b displays the Pt 4f core levels spectra of the calcined catalysts. For the Pt promoted catalyst (NiPt/HAp), the Pt $4f_{7/2}$ and Pt $4f_{5/2}$ are observed at around 73.7 and 77.1 eV, respectively. In the chemically activated catalysts (NiPt/KHAp and NiPt/SHAp) the Pt $4f_{7/2}$ peak appeared at higher BE values (73.9–74.1 eV). Binding values at around 72.4–72.8 eV of Pt $4f_{7/2}$ have been assigned to Pt^{2+} species, whereas values in the 73.7–74.3 eV have been ascribed to Pt^{4+} species deposited onto synthetic hydroxyapatite [48]. Thus, the obtained XPS data suggested a more oxidized state of $Pt^{\delta+}$ species (i.e. PtO_2 species) in the chemically activated samples. Moreover, the larger FWHM value corresponding to the Pt $4f_{7/2}$ peak of the acid activated catalysts indicated a higher heterogeneity in Pt environments. The coexistence of trace amounts of metallic Pt should not be discarded [49].

In the reduced samples, the XPS spectra of Ni $2p_{3/2}$ (Fig. 3c) showed a new and intense peak at around 852.4 eV, characteristic of metallic Ni, and another wide band in the 856.4–857.1 eV range, which denotes the existence of $Ni^{\delta+}$ species with strong interaction with the support or ion-exchanged. These results evidenced that Ni was partially reduced during the activation under hydrogen flow. On one hand, it can be deduced that chemical activation did not induce significant modification on the chemical environment of the metallic Ni supported onto the catalyst surface (similar BE value of 852.4 eV for all catalysts). On the other hand, the existence of some $Ni^{\delta+}$ species in the reduced catalyst could be ascribed to the existence of Ni particles in close interaction with the apatite support which were more difficult to reduce. The nanometric size of these particles would explain the absence in the XRD spectra. The XPS analysis of the reduced samples evidenced that Pt was fully reduced to metallic Pt as all samples exhibited Pt $4f_{7/2}$ features at around 70.5 eV [50]. Moreover, Pt promotion did not originate significant alteration in the oxidation state of $Ni^{\delta+}$ (857.1 eV for Ni/HAp and NiPt/HAp samples). However, in the chemically activated samples the feature of the Ni species peaked at lower BE values compared to the non-chemically treated samples (856.4–856.7), what suggested changes in the oxidation state of the $Ni^{\delta+}$ deposited onto catalyst surface.

Oxygen existed in two forms (Figure S5, ESI), as lattice oxygen (~530.3 eV) and hydroxides or defect oxide oxygen (~531.3 eV) [51]. Interestingly, values summarised in Table S4 (ESI) indicated that chemical activation modified the relative atomic amount of oxygen species, with a significant increase (from 53 to 56 at.% to 63–64 at.%) in oxygen defects.

Acid-base sites of the catalysts

Table 2 assembles the data obtained for NH_3 and CO_2 pulse chemisorption for all the reduced catalysts. After Pt-impregnation, the total number of acidic sites increased by around 25 % when compared to Ni/HAp. The sample treated with K_2CO_3 displayed the lowest total surface acidity, as could be expected. Interestingly, despite having used a strong acid, the acid activated NiPt/SHAp sample preserved acid sites density close to that of the reference sample (0.9 vs 0.93 sites/nm^2). The acidity per unit mass of the NiPt/SHAp sample compared to the reference sample has actually decreased due to acid impregnation (72.4 vs 106.7 $\mu mol_{NH3}/g_{cat}$). This impregnation partially dissolved the bioapatite and created a cation-deficient structure with reduced P-OH functionalities, which are precursors of acid centres [32]. The surface basicity decreased with Pt-doping. The change in the number of basic sites for the chemically treated samples ranged between −15.8 % and + 43.2 % when compared to the reference sample. In general, the catalysts have an amphoteric nature with acid and basic centres, with a slight predominance of acid centres over the basic ones in the untreated samples. Only after alkaline treatment this ratio reverted (basic/acid = 2.19 vs. 0.4–0.6) what could be ascribed to carbonates deposited on the catalyst surface, as inferred from TPR and FTIR results.

Catalytic activity

Fig. 4 compares the WGS performance of the prepared catalysts in the 200–450 °C range for a typical reformer outlet stream mixture (i.e. in the presence of both H_2 and CO_2). It can be observed that the Pt-promoted catalyst NiPt/HAp showed the highest activity, followed by the reference catalyst Ni/HAp. The former catalyst reached 32 % conversion of CO at around 300 °C and 80 % at 325 °C (Fig. 4a). The thermodynamic WGS equilibrium was reached at around 350 °C by these two catalysts. For the chemically treated catalysts (NiPt/SHAp and NiPt/KHAp), the light-off curve was slightly displaced to higher temperatures, reaching WGS equilibrium at 370 °C and 390 °C, respectively. For instance, at 325 °C, the CO conversion was 32 % and 51 %, respectively. If the T_{50} values are compared (Table 2), the WGS activity of the prepared catalysts varies as follows: NiPt/HAp > Ni/HAp > NiPt/KHAp > NiPt/SHAp. The lower specific surface area of the latter catalysts (35–45 % lower than those non-chemically activated) could partly explain this behavior.

The specific activity (r_{CO}) was measured at 275 °C in order to approach to differential reactor conditions (X_{CO} < 10 %). The most active catalyst was NiPt/HAp (Table 2, 6.7 $\mu mol_{CO}/g/s$) which showed 68 % higher activity than the reference catalyst (4.0 $\mu mol_{CO}/g/s$). Data from Table 2 reveal that NiPt/HAp contained the highest metallic sites (59.8×10^{18} at_{Metal}/g) among the Pt-doped samples (NiPt/HAp, NiPt/KHAp, NiPt/SHAp). However, it is worth outlining that the reference catalyst Ni/HAp contained the highest amount of exposed sites (77.1×10^{18} at_{Metal}/g), though, as previously noted, a lower specific activity. As revealed by XPS analyses of the reduced catalysts (Table S4, ESI), NiPt/HAp contained the maximum content of metallic Ni on the surface (39 at.%), and also, more surface oxygen defects. It seemed that the enhanced reducibility of the Pt-promoted catalysts caused some nanostructural modifications (i.e. increase oxygen defects) in the surface of the natural apatite which promote WGS activity [52]. It is likely that the Ni^{2+} and Pt^{1+} atoms exchanged in the apatite framework, leave the cationic sites after reduction, and generate surface vacancies in the support.

Regarding the WGS selectivity, it should be noted that methane was detected for all catalysts. The selectivity of the reaction to CH_4 and H_2 is illustrated in Fig. 4b,c. The methane and hydrogen formation profiles with respect to reaction temperature obtained by the catalysts supported on non-chemically treated HAp (Ni/HAp and NiPt/HAp) was similar. Methane formation began at around 275 °C and peaked at around 450 °C with a methane yield reaching a value of 40 % by both catalysts. Hydrogen yield showed negative values for these two catalysts, that is, under the reaction conditions, where CO_2 and H_2 were co-fed, hydrogen was rather consumed than generated in the reactor. In the literature, Ni-based catalysts were well reported as efficient catalysts for the reverse WGS (RWGS) [53,54]. As can be observed, the hydrogen production

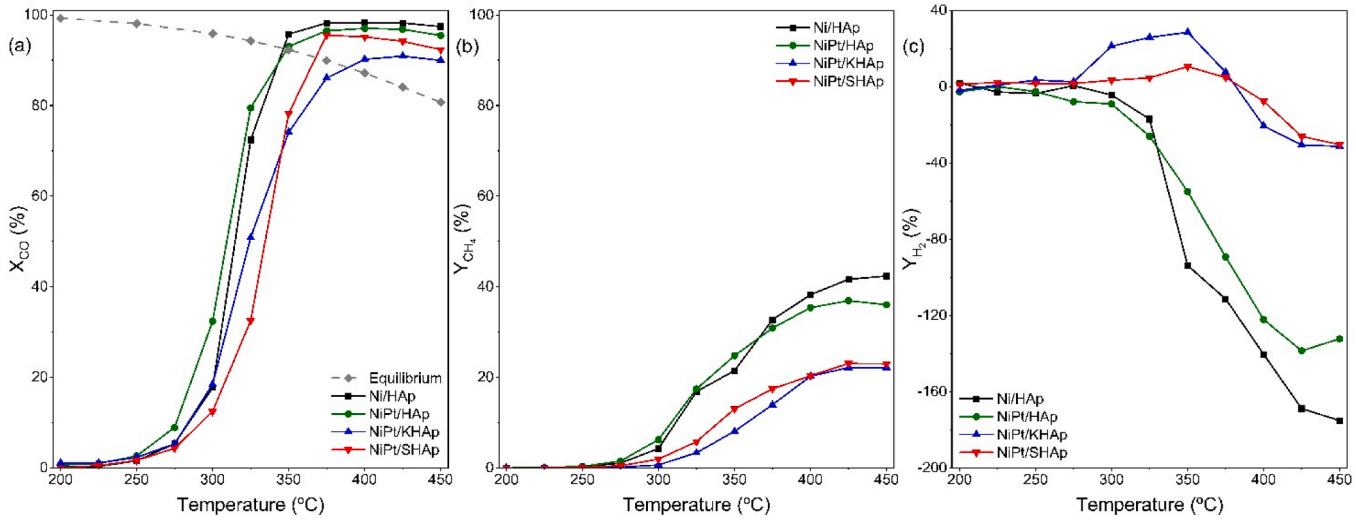

Fig. 4. Catalytic activity and selectivity in the WGS. (a) CO conversion light-off curve, (b) methane yield, (c) Hydrogen yield. (WGS reaction conditions: 5 % CO, 4 % CO_2, 31 % H_2, 14 % He, 46 % H_2O; GHSV of 120,000 h^{-1}).

yield followed a descending trend with temperature. Moreover, an abrupt change in slope (more negative) at above 325 °C occurred. It seemed that Pt-doping to Ni catalyst supported onto natural apatite did not significantly modify the selectivity of the WGS reaction. We may conclude that Pt enhanced WGS activity by increasing the amount of accessible Ni^0 sites and, likely by a favoured water dissociation on surface oxygen vacancies on the natural apatite [55,56].

It is worth noting that the reaction selectivity significantly varied for the chemically treated assays. On one hand, catalysts NiPt/KHAp and NiPt/SHAp were more selective to hydrogen production than the former catalysts. The methane yield was notably reduced by the chemically activated catalysts, with a maximum value, at around 425 °C (Y_{CH4} = 20 %), which is 50 % lower than that measured for the non-chemically activated samples (Y_{CH4} = 40 %). Likewise, by the chemically treated catalysts, the net hydrogen production became positive in a wide temperature range (Fig. 3c), in contrast to the negative hydrogen production by the non-treated assays.

The turnover frequency (TOF) normalized by surface active metal sites (measured by H_2 chemisorption), at 275 °C, are shown in Table 2. The TOF was lowest for the reference catalyst (0.03 s^{-1}) and increased with Pt-doping (TOF = 0.07 s^{-1}), that is, the metallic sites in the latter catalyst are two-fold more active than in the former. The chemical activation of the support with the alkali caused the reduction of the TOF (0.04 s^{-1}). Interestingly, the acid treated NiPt/SHAp catalyst gave the highest TOF value (0.10 s^{-1}), three-fold more active than the reference catalyst. The relatively high activity of the metallic sites spread on the surface on the natural apatite could be explained by the larger particle size and stronger interaction with the support [57]. Moreover, catalyst NiPt/SHAp contained more reactive sites on the apatite surface and also more OH^- sites (as assessed by FTIR) and more oxygen defects (as assessed by XPS). The role of hydroxyl groups on catalyst surfaces is widely recognised as significant for enhancing hydrogen production efficiency, since these groups facilitate the adsorption and dissociation of water, promoting reaction rate and catalyst stability [12,58]. The NiPt/KHAp catalyst, however, contained highly dispersed carbonate species. The abundance of such species would imply a close interaction with the Ni-Pt nanoparticles and likely lower their efficiency. This lower efficiency seemed to be compensated by the higher amount of exposed metal sites on the NiPt/KHAp catalysts, which could explain the increased overall activity (4.0 $\mu mol_{CO}/g/s$). The catalyst NiPt/SHAp contained the lowest amount of carbonates. Its performance is comparable to others reported in the literature (Table S5, ESI). Thus, the obtained values reveal that naturally obtained apatite is a suitable catalytic support for the WGS reaction.

The above mentioned low CH_4 and high H_2 selectivity and the observed benefit in the TOF value must be due to the physicochemical and structural properties of the support. As mentioned above, alkali and acid treatment modified the properties of the apatite. As revealed by the XRD study, crystal growing of both the apatite and the NiO phase were enhanced. Moreover, the growing geometry of the NiO nanoparticles was significantly increased in the horizontal plane by the acid activation. It seemed that the metallic nickel derived from the reduction of horizontal facets might have beneficial effects on the selectivity to H_2 in the WGS reaction. Senanayake et al. reported a preferential adsorption of physisorbed CO in the horizontal plane with respect to the surface [59] what could be related to the above observation.

Stability study

The stability of the catalysts was studied at isoconversional conditions (initial CO conversion in the 70–80 % range). Based on the WGS light-off curves, a temperature of 325 °C for Ni/HAp and NiPt/HAp and 350 °C for NiPt/KHAp and NiPt/SHAp were chosen, and the WGS reaction was conducted for 30 h time-on-stream (TOS). As can be observed in Fig. 5a, the reference catalyst showed a stable catalytic behaviour during the first 13 h of TOS. Afterwards, it suffered deactivation and CO conversion dropped-off by 52 % after 30 h of TOS. After Pt doping (NiPt/HAp) initial activity dropped by around 64 %, though it seemed to be more resistant with an activity loss of 15 % after 30 h TOS. Interestingly, acid treatment did not affect the CO conversion trend in the long-term run. As will be discussed later, a different outcome was observed in the selectivity data. Finally, catalyst NiPt/KHAp showed a high initial conversion of 77 %, though, a rapid and significant loss of activity occurred after 3 h TOS, ending with a 33 % loss of activity after 30 h TOS. A common feature of all the Pt-promoted catalysts was the good stability during the 30 h of reaction, thus, its positive effect on the apatite supported catalysts can be highlighted.

It is worth outlining the behaviour in the selectivity of these catalysts with TOS. Those supported onto the bare apatite (Ni/HAp, NiPt/HAp) showed a comparable evolution of the methane yield (Fig. 5b). They showed an initial value of Y_{CH4} = 14 % which progressively decreased with TOS to around 10 % after 30 h TOS. The chemically activated catalysts showed a distinct evolution between each other. The initial methane production by NiPt/KHAp and NiPt/SHAp was around 9 %, in line with data from the light-off curves. For the alkali-treated catalyst, the initial methane yield sharply increased during the first 5 h TOS (Y_{CH4}

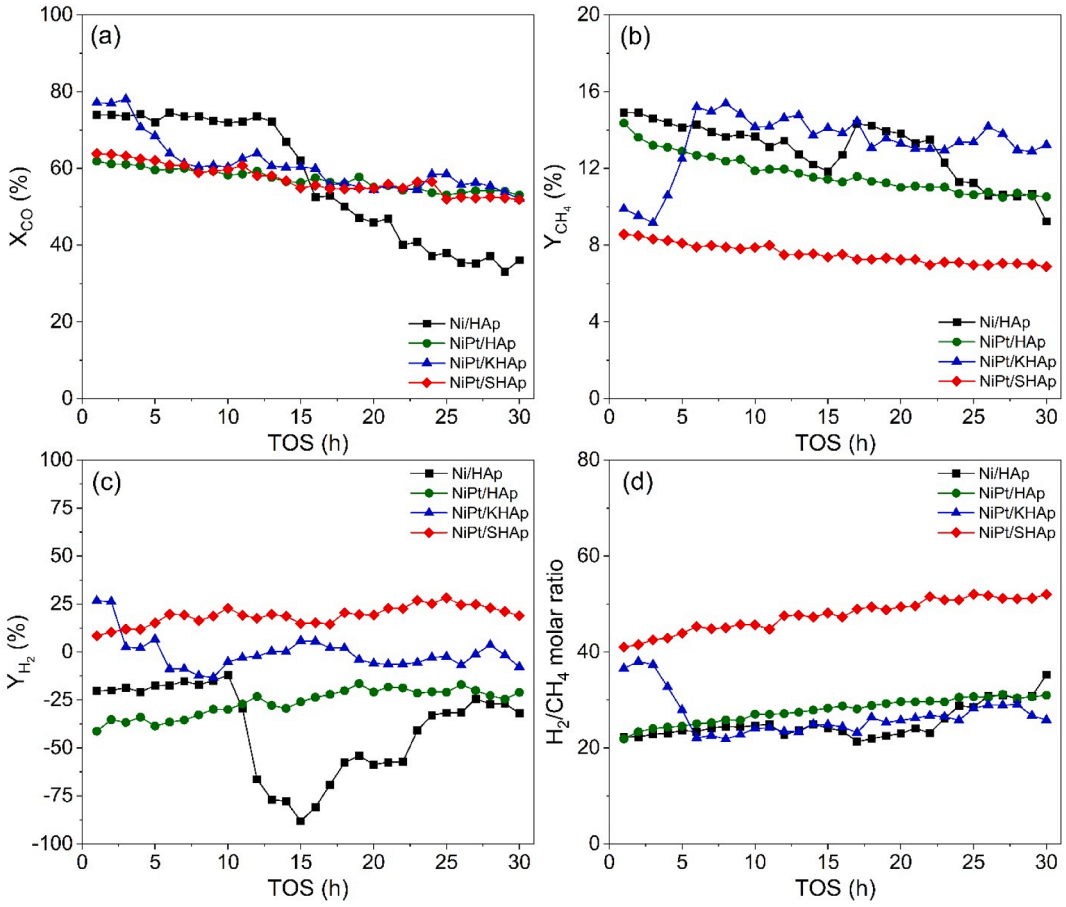

Fig. 5. (a) CO conversion, (b) methane yield, (c) hydrogen yield, and (d) H_2/CH_4 ratio in long-term tests obtained by different catalysts.

from 9 to 15 %). The acid treated assay, contrarily, showed a quasi-stable methane formation throughout all the catalytic run (Y_{CH4} = 7–8 %).

Fig. 5c shows the evolution of hydrogen yield with TOS. The reference catalyst Ni/HAp showed an initial negative net hydrogen production which became even more negative after 10 h of TOS, coinciding with the decline in the catalyst activity. Pt-doping decreased the selectivity to hydrogen, as revealed by Y_{H2} of catalysts NiPt/HAp which ranged from −40 to −20 % throughout all the run. The alkali-treated catalysts showed a high initial hydrogen yield (around 20 %), in line with previous light-off data (Fig. 4c). However, it deteriorated after 3 h of TOS. The catalyst NiPt/SHAp showed the most promising behaviour with a positive net hydrogen in the whole operation. It showed an initial value of around 10 % which even increased with TOS (to around 20 %, after 10 h TOS), coinciding with the above-mentioned decline in methanation activity. Zhou et al. [60] stated that the activation mode of hydrogen on single atoms depends on the local coordination environment, just like the interplay between ligands and metal centres in homogeneous organometallic chemistry. Indeed, the observed inverse correlation is consequence of the occurrence of CO and/or CO_2 hydrogenation to give methane. The H_2 to CH_4 molar ratio (H_2/CH_4) was used to analyse the reaction selectivity. The highest H_2/CH_4 were obtained by the acid activated assay (Fig. 5d). For this catalyst, H_2/CH_4 steadily increased from 40 to c.a. 50 after 30 h TOS. This ratio was about two-fold larger than that reached by the rest of catalysts in the long-term run. As noted above, catalyst NiPt/KHAp showed a distinct behaviour. The initial decrease in the H_2/CH_4 mole ratio could be derived from the boosting of the methanation activity, which is a hydrogen-consuming reaction. This behaviour might be related to its higher basic character (Table 2) which tend to retain the chemisorbed carbonaceous species.

Some reoxidation of the Ni particles could be deduced from XRD diffractogram of exhausted catalysts (Fig. 1c), basically in the non-chemically treated catalysts. It could be envisaged that the chemical activation could inhibit the aggregation of the Ni nanoparticles and promote the catalyst stability even under the high temperature conditions in the WGS reaction. It is also worth noting the formation of solid carbon, as deduced from the mass balance (Figure S6, ESI), specially, in the non-chemically treated assays. For instance, the solid carbon formation was low by the reference catalyst during the first 10 h of TOS (<5%), thereafter, abruptly increased to around 25 %. Such alteration can be linked to the chemical and textural instability of this catalyst. It seemed that the occurrence of the Boudouard reaction (Equation (5) might be favoured [34]. This reaction scheme would imply the simultaneous increase in CO_2 selectivity. However, as illustrated in Figure S6a (ESI), the selectivity to CO_2 of Ni/HAp decreased after 10 h TOS. The fact that the sharp change in the solid carbon (increase), CO_2 (decrease) and H_2 (decrease) selectivity took place simultaneously, suggested that all these species conformed a complex reaction mechanism. That is, the CO_2 formed from the Boudouard reaction could be readily consumed by the RWGS. Under the experimental conditions used in this work, CO formation from RWGS (Equation (1) is possible as predicted by thermodynamic calculations [61]. From results in Figs. 4-5 it seemed that RWGS mechanism was likely to occur for the reference catalyst Ni/HAp. Note that hydrogen and water were also co-fed for the WGS reaction tests. As previously noted, Pt-doping aimed to stabilize the catalytic behaviour, and selectivity to solid carbon was around 7 % for NiPt/HAp during 30 h TOS that lasted the run. The favourable interaction between Ni-Pt alloys and the carrier seemed to pose a clear effect on such behaviour and somewhat limited the methanation capacity. However, it seemed that the Boudouard reaction and RWGS reaction were favoured,

as deduced from the increase of carbon selectivity and decrease of CO_2 and H_2 selectivities of catalyst NiPt/HAp.

The catalyst prepared onto the alkali-treated bioapatite showed negative carbon selectivity values (around −3%). Such behaviour was likely due to gasification of carbonaceous material in the bioapatite. XPS data revealed that the atomic concentration of aliphatic C (C–C, C–H) on catalyst NiPt/KHAp was around three-fold larger than that in the other catalysts (Table S4 ESI, 6 % vs. c.a. 2 % C at.%). The observed initial rise in methane yield and the decline in CO_2 selectivity suggested the occurrence of hydrogenation reactions. Both CO and CO_2 can undergo hydrogenation to yield methane and water. The fluctuation in the CO conversion in Fig. 5a can be attributed to the blocking of the active sites by carbonaceous species on the NiPt/KHAp catalyst surface which likely decomposed/reacted during the course of the reaction [62]. Indeed, the CO species could be formed through the WGS reaction and simultaneously be consumed in methanation reaction.

Finally, the catalysts NiPt/SHAp showed low carbon selectivity (around 2 %) with quite a stable operation during 30 h of TOS. These results emphasize the suitability of acid activation of the bioapatite. The Ni-Pt alloying (shown by FESEM, SEM and mapping) and the adequate interaction of bimetallic particles with the surface not only enhanced the catalytic activity but also the suppression of carbon deposits during the WGS reaction. Note that H_2-TPR results revealed a strong metal-support interaction between the Ni and the acid treated apatite. Indeed, adequate chemical treatment of the apatite support has been proved to be an effective strategy to tailor the selectivity in the WGS reaction. Moreover, the acid treatment seemed to attenuate the undesired Boudouard and methanation reactions and drive the WGS reaction in the forward direction.

Conclusions

The synergistic effect of Pt-Ni has been addressed, as well as that of the chemical treatment of naturally derived hydroxyapatite (HAp) with H_2SO_4 or K_2CO_3. According to the characterization data, Pt-addition improved the reducibility of the Ni^{2+} species whereas chemical activation enhanced the textural-chemical stability of the catalysts. The alkali treatment enhanced the initial catalytic activity, presumably by increasing the surface basicity, which is known to be beneficial for the WGS reaction. However, the large amount of carbonate species on its surface caused the intense activity decay during the first hours of TOS. On the other hand, the acid-treated catalyst exhibited large NiO particles on the surface with preferential growth in the horizontal plane. However, the NiO species were in close interaction with the support. It was also discovered that acid treatment increased cation exchange.

The chemically activated samples were more selective to hydrogen production in WGS reaction with a feedstream similar to a reformer outlet. The acid-treated catalyst (NiPt/SHAp) showed the most stable behaviour during 30 h of TOS. Moreover, and contrary to bare catalyst, it sustained a positive net hydrogen production across the entire run, due to a lower extent of undesired reactions.

CRediT authorship contribution statement

U. Iriarte-Velasco: Conceptualization, Formal analysis, Writing – original draft, Funding acquisition. **M.A. Gutiérrez-Ortiz:** Resources, Funding acquisition, Supervision. **A.J. Reynoso:** Formal analysis, Validation, Writing – review & editing. **J.L. Ayastuy:** Investigation, Validation, Formal analysis, Data curation, Funding acquisition.

Declaration of competing interest

The authors declare that they have no known competing financial interests or personal relationships that could have appeared to influence the work reported in this paper.

Acknowledgments

This research was supported by grant PID2019-106692RB-I00 funded by MCIN/AEI/10.13039/501100011033 and the Basque Government (GV-2018-00038) is gratefully acknowledged. The authors also wish to express their gratitude for the technical and human support provided by SGIker of the UPV/EHU.

Appendix A. Supplementary material

Supplementary data to this article can be found online at https://doi.org/10.1016/j.jiec.2023.12.003.

References

[1] K. Mostakim, M.A. Arefin, M.T. Islam, K.M. Shifullah, M.A. Islam, Heliyon 7 (10) (2021) e08221.
[2] R.-R. Lee, I.-J. Jeon, W.-J. Jang, H.-S. Roh, J.-O. Shim, Catalysts 13 (4) (2023) 710, https://doi.org/10.3390/catal13040710.
[3] L. Zhou, Y. Liu, S. Liu, H. Zhang, X. Wu, R. Shen, T. Liu, J. Gao, K. Sun, B. Li, J. Jiang, J. Energy Chem. 83 (2023) 363–396, https://doi.org/10.1016/j.jechem.2023.03.055.
[4] R. Alshareef, M.A. Nahil, P.T. Williams, Energ. Fuel. 37 (5) (2023) 3894–3907, https://doi.org/10.1021/acs.energyfuels.2c02934.
[5] S. Prasad, K. Kumar-Yadav, S. Kumar, N. Gupta, M.M.S. Cabral-Pinto, S. Rezania, N. Radwan, J. Alam, J. Environ. Manage. 285 (2021), 112174, https://doi.org/10.1016/j.jenvman.2021.112174.
[6] M.I. Ariëns, L.G.A. van de Water, A.I. Dugulan, E. Brück, E.J.M. Hensen, ACS Catal. 12 (22) (2022) 13838–13852, https://doi.org/10.1021/acscatal.2c03871.
[7] A. Haryanto, S.D. Fernando, S.D. Filip To, P.H. Steele, L. Pordesimo, S. Adhikari, Energ. Fuel. 23 (6) (2009), 3097-3102. 10.1021/ef801076r.
[8] Y. Wang, N. Li, M. Chen, D. Liang, C. Li, Q. Liu, Z. Yang, J. Wang, Chin. J. Chem. Eng. 48 (2022) 176–190, https://doi.org/10.1016/j.cjche.2021.11.004.
[9] M. Chen, X. Feng, Y. Wang, D. Liang, C. Li, Z. Yang, J. Wang, Fuel 346 (2023), 128373, https://doi.org/10.1016/j.fuel.2023.128373.
[10] Y. Wang, S. Zhu, J. Lu, S. He, H. Lu, D. Song, D. Chen, Y. Luo, Fuel Process. Technol. 243 (2023), 107677, https://doi.org/10.1016/j.fuproc.2023.107677.
[11] U. Iriarte-Velasco, J.L. Ayastuy, Z. Boukha, R. Bravo, M.A. Gutiérrez-Ortiz, Renew. Energ. 115 (2018) 641–648, https://doi.org/10.1016/j.renene.2017.08.086.
[12] T. Noor, Y. Qi, D. Chen, Appl. Catal. B: Environ. 264 (2020), 118430, https://doi.org/10.1016/j.apcatb.2019.118430.
[13] K.-R. Hwang, C.-B. Lee, J.-S. Park, J. Power Sources 196 (3) (2011) 1349–1352, https://doi.org/10.1016/j.jpowsour.2010.08.084.
[14] J. Ashok, M.H. Wai, S. Kawi, ChemCatChem 10 (2018) 3927, https://doi.org/10.1002/cctc.201800031.
[15] X. Gao, X. Lin, X. Xie, J. Li, X. Wu, Y. Lia, S. Kawi, React. Chem. Eng. 7 (2022) 551–565, https://doi.org/10.1039/D1RE00537E.
[16] T. Wang, M.D. Porosoff, J.G. Chen, Catal. Today 233 (2014) 61–69, https://doi.org/10.1016/j.cattod.2013.09.037.
[17] T. Rajesh, A.K. Rajarajan, C.S. Gopinath, R.N. Devi, J. Phys. Chem. C 116 (17) (2012) 9526–9532, https://doi.org/10.1021/jp212211d.
[18] Y. Shu, X. Ma, X. Duan, D. Liu, L. Wang, Q. Niu, P. Zhang, Chem. Eng. Sci. 261 (2022), 117959, https://doi.org/10.1016/j.ces.2022.117959.
[19] M.L. Ang, U. Oemar, E.T. Saw, L. Mo, Y. Kathiraser, B.H. Chia, S. Kawi, ACS Catal. 4 (9) (2014) 3237–3248, https://doi.org/10.1021/cs500915p.
[20] M.D. Porosoff, J.G. Chen, J. Catal. 301 (2013) 30–37, https://doi.org/10.1016/j.jcat.2013.01.022.
[21] X.-C. Sun, K. Yuan, W.-D. Hua, Z.-R. Gao, Q. Zhang, C.-Y. Yuan, H.-C. Liu, Y.-W. Zhang, ACS Catal. 12 (19) (2022) 11942–11954, https://doi.org/10.1021/acscatal.2c03664.
[22] S. Navarro-Jaén, F. Romero-Sarria, M.A. Centeno, O.H. Laguna, J.A. Odriozola, Appl. Catal. B: Environ. 244 (2019) 853–862, https://doi.org/10.1016/j.apcatb.2018.12.022.
[23] B. Li, X. Yuan, B. Li, X. Wang, Fuel Process. Technol. 202 (2020), 106359, https://doi.org/10.1016/j.fuproc.2020.106359.
[24] Z. Wang, D. Ren, S. Shang, S. Zhang, X. Zhang, W. Chen, Adv. Powder Technol. 33 (3) (2022), 103509, https://doi.org/10.1016/j.apt.2022.103509.
[25] D. Miao, A. Goldbach, H. Xu, ACS Catal. 6 (2) (2016) 775–783, https://doi.org/10.1021/acscatal.5b01909.
[26] U. Iriarte-Velasco, J.L. Ayastuy, R. Bravo, Z. Boukha, M.A. Gutiérrez-Ortiz, J. Mater. Sci. 56 (2021) 6745–6763, https://doi.org/10.1007/s10853-020-05724-x.
[27] Z. Boukha, J.R. González-Velasco, M.A. Gutiérrez-Ortiz, Appl. Catal. B: Environ. 270 (2020), 118851, https://doi.org/10.1016/j.apcatb.2020.118851.
[28] U. Iriarte-Velasco, I. Sierra, M.A. Gutiérrez-Ortiz, J.L. Ayastuy, J. Environ. Chem. Eng. 11 (5) (2023), 110677, https://doi.org/10.1016/j.jece.2023.110677.
[29] Y. Sa, Y. Guo, X. Feng, M. Wang, P. Li, Y. Gao, X. Yang, T. Jiang, New J. Chem. 41 (2017) 5723–5731, https://doi.org/10.1039/C7NJ00803A.
[30] U. Tariq, Z. Haider, K. Chaudhary, R. Hussain J. Ali, J. Phys.: Conf. Ser. 1027, 012015. 10.1088/1742-6596/1027/1/012015.
[31] I. Cacciotti, Cationic and Anionic Substitutions in Hydroxyapatite. In: Antoniac, I. (eds) Handbook of Bioceramics and Biocomposites. Springer, Cham. 2016. .

[32] I. Sierra, J.L. Ayastuy, M.A. Gutiérrez-Ortiz, U. Iriarte-Velasco, J. Anal. Appl. Pyrolysis 171 (2023), 105973, https://doi.org/10.1016/j.jaap.2023.105973.
[33] J. Meng, W. Pan, T. Gu, C. Bu, J. Zhang, X. Wang, C. Liu, H. Xie, G. Piao, Energy Fuels 35 (23) (2021) 19568–19580, https://doi.org/10.1021/acs.energyfuels.1c02851.
[34] T.S. Phan, A.R. Sane, B.Rêgo de Vasconcelos, A. Nzihou, P. Sharrock, D. Grouset, D. Pham Minh, Appl. Catal. B: Environ. 224 (2018) 310-321. 10.1016/j.apcatb.2017.10.063.
[35] R. Titorenkova, E. Dyulgerova, V. Petkova, R. Ilieva, Ceram. Int. 45 (6) (2019) 7025–7033, https://doi.org/10.1016/j.ceramint.2018.12.204.
[36] Z. Boukha, A. Bermejo-López, B. Pereda-Ayo, J.A. González-Marcos, J.R. González-Velasco, Appl. Catal. B: Environ. 314 (2022), 121500, https://doi.org/10.1016/j.apcatb.2022.121500.
[37] Z. Boukha, M.P. Yeste, M.A. Cauqui, J.R. González-Velasco, Appl. Catal. A: Gen. 580 (2019) 34–45, https://doi.org/10.1016/j.apcata.2019.04.034.
[38] Z. Boukha, M. Kacimi, M.F.R. Pereira, J.L. Faria, J.L. Figueiredo, M. Ziyad, Appl. Catal. A: Gen. 317 (2) (2007) 299–309, https://doi.org/10.1016/j.apcata.2006.10.029.
[39] A. Tanksale, J.N. Beltramini, J.A. Dumesic, G.Q. Lu, J. Catal. 258 (2) (2008) 366–377, https://doi.org/10.1016/j.jcat.2008.06.024.
[40] L. Guo, Y. Tian, X. He, C. Qiao, G. Liu, Fuel 322 (2022), 124082, https://doi.org/10.1016/j.fuel.2022.124082.
[41] J. Lyu, Y. Tian, Y. Zhang, P. Wu, Y. Pan, T. Ding, S. Song, X. Li, Catal. Sci. Technol. 12 (2022) 4675–4678, https://doi.org/10.1039/D2CY00952H.
[42] Z. Xu, G. Huang, Z. Yan, N. Wang, L. Yue, Q. Liu, ACS Omega 4 (26) (2019) 21998–22007, https://doi.org/10.1021/acsomega.9b03068.
[43] E. Landi, G. Celotti, G. Logroscino, A. Tampieri, J. Eur. Ceram. Soc. 23 (15) (2003) 2931–2937, https://doi.org/10.1016/S0955-2219(03)00304-2.
[44] W. You, M. Wang, W. Lam, W. Yuk, Tissue Eng. Intech (2010), https://doi.org/10.5772/8574.
[45] H. Du, C.T. Williams, A.D. Ebner, J.A. Ritter, Chem. Mater. 22 (11) (2010) 3519–3526, https://doi.org/10.1021/cm100703e.
[46] L. Yang, M.P. Bukhovko, A. Malek, L. Li, C.W. Jones, P.K. Agrawal, R.J. Davis, Appl. Catal A: Gen. 603 (2020), 117739, https://doi.org/10.1016/j.apcata.2020.117739.
[47] W. Pan, J. Meng, T. Gu, Q. Zhang, J. Zhang, X. Wang, C. Bu, C. Liu, H. Xie, G. Piao, Fuel 339 (2023), 127327, https://doi.org/10.1016/j.fuel.2022.127327.
[48] D. Miao, G. Cavusoglu, H. Lichtenberg, J. Yu, H. Xu, J.-D. Grunwaldt, A. Goldbach, Appl. Catal. B: Environ. 202 (2017) 587–596, https://doi.org/10.1016/j.apcatb.2016.09.059.
[49] W. Xie, Z. Huang, R. Wang, C. Wen, Y. Zhou, J. Mater. Sci. 55 (2020) 11829-11840. .
[50] Y. Ouyang, H. Cao, H. Wu, D. Wu, F. Wang, X. Fan, W. Yuan, M. He, L. Ying Zhang, C. Ming Li, Appl. Catal. B: Environ. 265 (2020) 118606. 10.1016/j.apcatb.2020.118606.
[51] H. Idriss, Surf. Sci. 712 (2021), 121894, https://doi.org/10.1016/j.susc.2021.121894.
[52] J. Vecchietti, A. Bonivardi, W. Xu, D. Stacchiola, J.J. Delgado, M. Calatayud, S. E. Collins, ACS Catal. 4 (6) (2014) 2088–2096, https://doi.org/10.1021/cs500323u.
[53] L. Wang, H. Liu, Y. Chen, S. Yang, Int. J. Hydrog. Energy 42 (6) (2017) 3682–3689, https://doi.org/10.1016/j.ijhydene.2016.07.048.
[54] R.V. Gonçalves, L.L.R. Vono, R. Wojcieszak, C.S.B. Dias, H. Wender, E. Teixeira-Neto, L.M. Rossi, Appl. Catal. B: Environ. 209 (2017) 240–246, https://doi.org/10.1016/j.apcatb.2017.02.081.
[55] R.J. Gorte, S. Zhao, Catal. Today 104 (1) (2005) 18–24, https://doi.org/10.1016/j.cattod.2005.03.034.
[56] G. Jacobs, B.H. Davis, Int. J. Hydrog. Energy 35 (8) (2010) 3522–3536, https://doi.org/10.1016/j.ijhydene.2010.01.055.
[57] J.F.M. Simons, T.J. de Heer, R.C.J. van de Poll, V. Muravev, N. Kosinov, E.J. M. Hensen, J. Am. Chem. Soc. 145 (2023) 37, https://doi.org/10.1021/jacs.3c04284.
[58] Y. Li, M. Kottwitz, J.L. Vincent, M.J. Enright, Z. Liu, L. Zhang, J. Huang, S. D. Senanayake, W.-C.-D. Yang, P.A. Crozier, R.G. Nuzzo, A.I. Frenkel, Nat. Commun. 12 (2021) 914, https://doi.org/10.1038/s41467-021-21132-4.
[59] S.D. Senanayake, J. Evans, S. Agnoli, L. Barrio, T.-L. Chen, J. Hrbek, J. A. Rodriguez, Top. Catal. 54 (2011) 34–41, https://doi.org/10.1007/s11244-011-9645-6.
[60] M. Zhou, M. Yang, X. Yang, X. Zhao, L. Sun, W. Deng, A. Wang, J. Li, T. Zhang, Chinese J. Catal. 41 (3) (2020) 524–532, https://doi.org/10.1016/S1872-2067(19)63517-5.
[61] M.A. Soria, C. Mateos-Pedrero, A. Guerrero-Ruiz, I. Rodríguez-Ramos, Int. J. Hydrog. Energy 36 (23) (2011) 15212–15220, https://doi.org/10.1016/j.ijhydene.2011.08.117.
[62] M. Khoshtinat Nikoo, N.A.S. Amin, Fuel Process. Technol. 92 (3) (2011) 678-691. 10.1016/j.fuproc.2010.11.027.